Nano-Hybrids Based on Surface Modified Reduced Graphene Oxide Nanosheets and Carbon Nanotubes and a Regioregular Polythiophene

Samira Agbolaghi[*,1], Saleheh Abbaspoor[2]*

[1]*Chemical Engineering Department, Faculty of Engineering, Azarbaijan Shahid Madani University, Tabriz, Iran.*

[2]*Faculty of Polymer Engineering and Institute of Polymeric Materials, Sahand University of Technology, Tabriz, Iran.*

ABSTRACT

The multi-walled carbon nanotubes (CNTs) and reduced graphene oxide (rGO) nanosheets were functionalized with 2-hydroxymethyl thiophene (CNT-f-COOTh) and 2-thiophene acetic acid (rGO-f-TAA) and grafted with poly(3-dodecylthiophene) (CNT-g-PDDT and rGO-g-PDDT) to manipulate the orientation and patterning of crystallized regioregular poly(3-hexylthiophene) (P3HT). Distinct nano-hybrid structures including double-fibrillar (5.11–5.18 S/cm), shish-kebab (2.19–2.28 S/cm), and stem-leaf (6.96–7.51 S/cm) were developed using modified CNTs and P3HT. The most effective parameter on morphology of donor-acceptor supramolecules was the surface functionalization and grafting. The electrical conductivities of supramolecules based on P3HT and rGO, rGO-f-TAA, and rGO-g-PDDT ranged in 3.81–3.87, 3.91–3.95, and 10.67–10.70 S/cm, respectively. P3HT chains preferred to interact with their thiophene rings with bared rGO and CNT surfaces, resulting in a conventional face-on orientation. In P3HT/rGO-f-TAA and P3HT/CNT-f-COOTh supramolecular nanostructures patterned with P3HT, the orientation of P3HT chains changed from face-on to edge-on, originating from the strong interactions between the hexyl side chains of P3HTs and functional groups. Nano-hybrids based on grafted rGO demonstrated a patched-like morphology composed of flat-on P3HTs with main backbones perpendicular to the substrate. Based on the ultraviolet-visible and photoluminescence analyses, the flat-on orientation was the best for P3HT chains assembled onto CNT and rGO, which was acquired for CNT-g-PDDT and rGO-g-PDDT nano-hybrids.

Keywords: Carbon nanotube; Reduced Graphene Oxide, Orientation, Grafting, Functionalization, Nano-hybrid.

1. Introduction

The common orientations for poly(3-hexylthiophene) (P3HT) chains are the edge-on (with the main backbones parallel with and side chains perpendicular to the substrate) and face-on (with both main backbones and side chains parallel with the substrate). Another orientation called flat-on with the backbones perpendicular to the substrate and the highest conductivity and hole mobility was obtained with some especial protocols. Among the mentioned orientations, the edge-on has the highest potential in the field effect transistors, due to their horizontal configuration with in-plane charge mobility. On the contrary, the photovoltaic devices such as solar cells with the vertical configuration and out-of plane charge mobility further benefit from the face-on orientation [1−9].

Graphene is one of carbon allotropes which is composed of two dimensional carbon arrangements with sp^2 hybridation in the form of hexagonal honeycomb. The unique structure of graphene leads to a charge carrier independent of temperature around 10^4 cm^2/V.s, which is four order of magnitude larger than that of phenyl-C-butyric acid methyl ester (PCBM) at room temperature [10–22]. The carbon nanotubes could be also considered as a roll of graphene, thereby with a similar electrical, mechanical, and thermal characteristics but possessing different surface area and energy. Graphene for the high electron mobility, conductivity and elasticity and facile inclusion into the polymeric matrix has attracted a great attraction [23–25]. Reduced graphene oxide (rGO) is a cheap alternative for graphene whose production in nano-scale and high contents is difficult [10,26]. Graphene for having a high surface area could be employed as an ideal substrate to attach the functionalized materials and fabricate the hybrid structures. Moreover, the unique electrical, thermal, and mechanical properties of graphene provide an opportunity to utilize it in the high efficient electronic devices such as photovoltaics, sensors, etc [27–37]. The transparency of single and also multilayer graphenes is an advantage in the optoelectronic applications, in which the light diffuses into the inner layers [3,38]. Recently, it has been proved that graphene can be used as an electron acceptor in the photovoltaic devices [2,13,39,40]. The field effect transistors and solar cells based on graphene have been also reported in the literature [15,36,37].

Based on conducted studies on the induced crystallization of poly(3-alkylthiophene) (P3AT) onto graphene [26,41,42] such as well-oriented ultrathin P3HT films on graphene having face-on and edge-on orientations [3], connecting the individual rGO monolayers with P3HT nanowires [26], semi-spherulites composed of nanoribbons prepared by aging the GO/P3BT mixture [27], etc, a gap is sensed in the oriented crystallization of P3HT on the functionalized and grafted graphenes.

Carbon nanotubes (CNTs) are one-dimensional (1D) nanostructured carbon allotropes with high carrier mobility and unique ballistic conduction pathways [43]. The band gap of CNTs can be adjusted by controlling the diameter and chirality [44–46]. They are classified as single-walled (SWCNT) and multi-walled (MWCNT) nanotubes depending on the number of folds present in the tube [47–50]. Owing to their extraordinary electrical and mechanical properties, CNTs are extensively employed as charming nanomaterials [51,52]. The CNTs have a wide range of applications including photovoltaic devices, sensors, and field-effect transistors [53–58], because of their unique electrical, mechanical, high electrical conductivity, large specific surface area, and high charge capacitance properties [59]. Thanks to their high hydrophobicity, the CNTs are not easily processed [60]. The surface carbon atoms in nanotubes present an excellent platform for chemical functionalization, and have been utilized to address the processability issue. The direct polymerization of monomers in CNT-dispersed medium through functionalization of CNT has achieved great attention to prepare polymer wrapped CNTs [61–63]. Various polymers were successfully grafted onto CNT to develop CNT-polymer composites with an improved dispersion [64–68]. Some technical analyses including grazing incidence wide angle X-ray scattering (GIWAXS) [69], in situ small angle X-ray scattering (SAXS) [70], and plasmon resonance [71] are also applied for characterizing the carbonic colloids and the other colloidal nanoparticles.

In the current work, the donor-acceptor nano-hybrids were designed by functionalization and grafting of CNT and rGO surface with thiophenic adducts. Distinct well-oriented nano-hybrids comprising double-fibrillar in unmodified CNTs, shish-kebab in functionalized CNTs (CNT-f-COOTh) and stem-leaf in grafted CNTs (CNT-g-PDDT) were designed and compared with the corresponding rGO nanostructures. Despite the fact that the P3HT orientations depended on the surface modification, their morphologies were altered in rolled (CNT) and flat (rGO) carbonic surfaces.

2. Experimental
2.1 Thiophene functionalized carbon nanotubes (CNT-f-COOTh)

Functionalization of MWCNTs was carried out via oxidation method with sonication of sulfuric acid (15 mL, 95–97 %) and nitric acid (45 mL, 65 %) having a ratio of 1:3 v/v for 6 h at 50 °C. A five-fold dilution was then applied to the mixture for stopping the oxidation reaction. Stirring and decantation were performed for five times and finally washed with deionized water by filtration until the water pH reached 7. The precipitate was finally dried in

vacuum oven at 60 °C. The CNTs-COOH with high oxidation was synthesized by the same procedure for 9 h at 60 °C. The 2-hydroxymethyl thiophene (CNT-COOH-f-HMTh) macroinitiator was synthesized by the esterification of CNT-COOH with 2-hydroxymethyl thiophene in the presence of p-toluenesulfonic acid (p-TSA) as a dehydrating agent (5 wt% of acid). In brief, a three-neck flask equipped with a dean-stark trap, gas inlet/outlet, and a magnetic stirrer was charged with CNT-COOH (0.5 g), 2-hydroxymethyl thiophene (1 g) and anhydrous dimethyl sulfoxide (50 mL), and then was sonicated with a bath type sonicator for 40 min to produce a homogeneous suspension. A catalytic amount of p-TSA as a dehydrating agent was added to the flask, and the reaction mixture was de-aerated by bubbling highly pure argon for 10 min. Thereafter, the flask was placed in a silicon oil bath at 140 °C and the reaction mixture was stirred for 6 h under argon atmosphere. The reaction water was removed as an azeotrope until no more water was formed. The suspension was then centrifuged and washed several times with methanol for remove of remaining 2-hydroxymethyl thiophene. The

(a)

(b)

Fig. 1- FT-IR spectra of CNT-f-COOTh and CNT-g-PDDT (a); rGO-f-TAA and rGO-g-PDDT (b).

CNT-COOH-f-HMTh powder (CNT-f-COOTh) was obtained after drying in reduced pressure at 60 °C. FT-IR spectrum of CNT-f-COOTh is depicted in Figure 1(a). In FT-IR spectrum of the thiophene functionalized carbon nanotubes (CNT-f-COOTh), the vibrational peaks originating from the stretching of C–S and C=O were observed at around 715 and 1656 cm^{-1}, respectively. The most important bands in FT-IR spectrum of CNT-g-PDDT were the weak aromatic α and β hydrogens of thiophene rings at 3000–3100 cm^{-1}, γ(C–H) in the aromatic ring at 719 cm^{-1}, the aromatic C=C stretching vibration at 1423, 1512 cm^{-1} and C–S stretching vibration in thiophene rings at 702 cm^{-1}. Further vibration from the CH-aliphatic bonds could be detected at around 2800–2950 cm^{-1}.

2.2 Chemical oxidative graft polymerization of 3-dodecylthiophene from multi-walled carbon nanotubes (CNTs-g-PDDT).

A 100 mL flask equipped with a condenser, dropping funnel, gas inlet/outlet and a magnetic stirrer was charged with CNTs-COOH-f-HMTh (0.5 g) and dried CHCl$_3$ (30 mL), and then was sonicated with a bath type sonicator for 40 min to reach a homogeneous suspension. Hereafter, 3-dodecylthiophene monomer (1.5 g) was added and the reaction mixture was deaerated by bubbling highly pure argon for 5 min. In a parallel system, 5 g of anhydrous ferric chloride was dissolved in 20 mL of dried acetonitrile. This solution was also deaerated and then slowly added to the reaction mixture at a rate of 5 mL min^{-1} under an argon atmosphere. The reaction mixture was refluxed for about 24 h at room temperature under an inert atmosphere. The reaction was terminated by pouring the flask content into a large amount of methanol. The product was filtered and washed several times with methanol. The dark color solid was dried in vacuum at room temperature. The crude product was extracted with CHCl$_3$ in a Soxhlet for 24 h to remove pure poly(3-dodecyl thiophene). The polymer solution was filtered, precipitated into excess methanol, and dried in reduced pressure to reach a dark color powder. The CNTs-g-PDDT possessing a high density of grafted thiophene (HD GCNT) was synthesized by the same method but with appropriate amounts of HD CNTs-COOH-f-HMTh (0.5 g), 3-dodecylthiophene monomer (3 g), and anhydrous ferric chloride (10 g). FT-IR spectrum of CNT-g-PDDT is depicted in Figure 1(a). After graft polymerization of thiophene
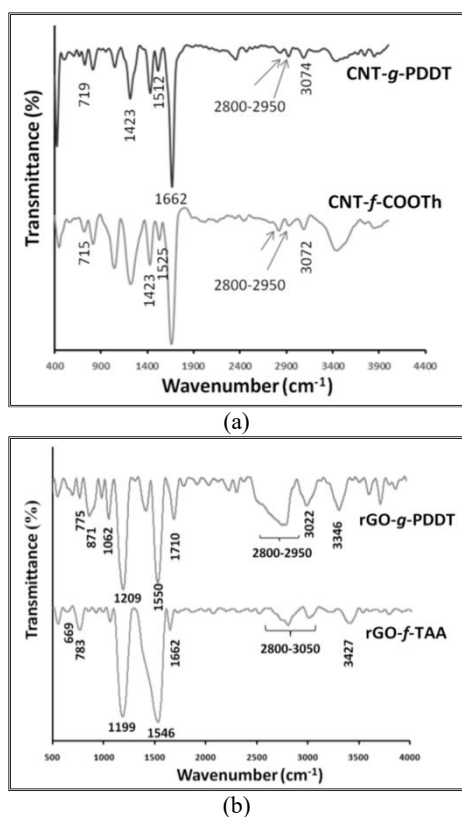
derivatives onto functionalized CNTs (CNT-g-PDDT), an increase was observed in the intensity of bands related to the polythiophene derivatives; however, the intensity of peaks attributed to MWCNTs decreased due to their low concentration in the grafted hybrid.

2.3 Functionalization of rGO with 2-thiophene acetic acid (rGO-f-TAA)

The rGO-f-TAA was synthesized by the esterification of rGO with 2-thiophene acetic acid in the presence of p-TSA as a dehydrating agent. Briefly, a three-neck flask equipped with a dean-stark trap, gas inlet/outlet, and a magnetic stirrer was charged with rGO (0.2 g), 2-thiophene acetic acid (2.1 g), and anhydrous dimethyl sulfoxide (100 mL), and then was sonicated for 40 min to produce a homogeneous suspension. A catalytic amount of p-TSA (0.2 g) as a dehydrating agent was added to the flask, and the reaction mixture was de-aerated by bubbling highly pure argon for 10 min. Thereafter, the flask was placed in a silicon oil bath at 140 °C, and the reaction mixture was stirred for 6 hours under argon atmosphere. The water of the reaction was removed as an azeotrope until no more water was formed, indicating the completion of reaction. Then, the suspension was centrifuged and washed several times with methanol to remove the remaining 2-thiophene acetic acid. The rGO-f-TAA powder was obtained after drying in reduced pressure at 60 °C. FT-IR spectrum of rGO-f-TAA is reported in Figure 1(b). The successful synthesis of rGO-TAA was verified by the appearance of new bands including the stretching vibrations of aliphatic and aromatic C–H at 3050–2800 cm^{-1}, γ(C–H) in the aromatic ring at 669 and 783 cm^{-1}, unreacted hydroxyl end groups as a broad strong band centered at 3427 cm^{-1}, and the aromatic C=C stretching vibration at 1546 cm^{-1}. Moreover, the band at 1662 cm^{-1} may be attributed to the carbonyl stretching vibration of 2-thiopheneacetate groups (Figure 1(b)).

2.4 Synthesis of rGO-g-PDDT via chemical oxidation polymerization

A 100 mL three-neck flask equipped with a condenser, dropping funnel, gas inlet/outlet, and a magnetic stirrer was charged with rGO-f-TAA (1.0 g) and dried CHCl$_3$ (90 mL), and then was sonicated for 40 min to produce a homogeneous suspension. Hereafter, the synthesized 3-dodecylthiophene monomer (3.5 g) was added and the reaction

mixture was deaerated by bubbling highly pure argon for 10 min. In a separate container, 10.0 g of anhydrous ferric chloride was dissolved in 30 mL of dried acetonitrile. This solution was deaerated by bubbling highly pure argon for 10 min, and then slowly added to the reaction mixture at a rate of 5 mL min^{-1} under an argon atmosphere. The reaction mixture was refluxed for 24 h at room temperature under an inert atmosphere. The reaction was terminated by pouring the content of the flask into a large amount of methanol, and the product was filtered and washed several times with methanol. The dark solid was dried in vacuum at room temperature, and the crude product was extracted with CHCl$_3$ in a Soxhlet apparatus for 24 h to remove pure poly(3-dodecyl thiopene). Synthesized rGO-g-PDDT was not soluble in hot CHCl$_3$, while pure poly(3-dodecyl thiopene) was soluble in this solvent. The polymer solution was filtered, precipitated into excess methanol, and dried in reduced pressure to give a dark powder. FT-IR spectrum of rGO-g-PDDT is reported in Figure 1(b). The most important bands in FT-IR spectrum of rGO-g-PDDT consisted of the weak aromatic α and β hydrogens of thiophene rings at 3050 to 3000 cm^{-1} region, γ(C–H) in the aromatic ring at 775 cm^{-1}, the aromatic C=C stretching vibration at 1423 cm^{-1}, and C–S stretching vibration at 678 cm^{-1} in thiophene rings. The successful grafting of PDDT onto rGO-TAA was verified by the appearance of new bands such as stretching vibration of carbonyl group at 1710 cm^{-1}, C–O stretching vibrations at 1209 cm^{-1}, and the stretching vibrations of aliphatic and aromatic C–H at 3050 to 2800 cm^{-1}.

2.5 Synthesis of regioregular P3HT via Grignard metathesis polymerization

Highly regioregular P3HT (> 99%) with the molecular weight (M$_n$) of 30 kDa and the polydispersity index (PDI) of 1.18 was synthesized through Grignard metathesis polymerization [54].

2.6 Sample preparation

The derivatives of CNTs comprising bared CNT, CNT-f-COOTh, and CNT-g-PDDT were mixed with DMF and toluene and subjected to different steps of dissolution, stirring, and crystallization. After addition of regioregular P3HT (RR-P3HT) chains to the vial, purging with high pure nitrogen, and performing the dissolution and stirring steps, the color of vial content turned to light orange for DMF and dark orange for

toluene. The concentration was 0.01 wt% and the ratio of P3HT:CNT, P3HT:CNT-f-COOTh, and P3HT:CNT-g-PDDT was 5:1. First, a primary dissolution was conducted at T_{d1} = 70 °C for 20 min (t_{d1}). The sonication step was then performed at 75 °C for 3 h using a Cup Horn Ultrasonic Convertor to yield the homogeneous dispersions. A secondary dissolution was carried out at 100 °C (T_{d2}) for 20 min (t_{d2}) in DMF to eliminate the probable effect of stirring on the P3HT crystallization. Finally, the vials were switched to 30 °C for 1 and 20 h to complete the crystallization.

Prepared materials including bared rGO, rGO-f-TAA, and rGO-g-PDDT were mixed with various solvents of DMF and toluene in a vial and subjected to distinct steps, i.e., dissolution, stirring, and crystallization. After addition of P3HT to the vial, purging with high pure nitrogen, and performing the dissolution and stirring steps, the color of vial content turned to light orange for DMF and DMF/toluene solvents and dark orange for toluene. The concentration was 0.01 wt% and the ratio of P3HT:rGO, P3HT:rGO-f-TAA, and P3HT:rGO-g-PDDT was 5:1. First, a primary dissolution was conducted at T_{d1} = 70 °C for 20 min (t_{d1}). Stirring was then performed at 75 °C for 3 h to yield the homogeneous dispersions. A secondary dissolution was carried out at 100 ° for 20 min in DMF to eliminate the probable effect of stirring on the P3HT crystallization. Finally, the vials were switched to 30 °C for 1 and 20 h to complete the crystallization.

2.7 Characterization

The donor-acceptor supramolecules were characterized with Lambda 750 ultraviolet-visible (UV-Vis) spectrometer, photoluminescence optistatDry-BLV model, atomic force microscope (AFM Nanoscope), transmission electron microscope (Philips CM30 TEM) equipped with the selected area electron diffraction (SAED) and grazing incidence wide angle X-ray scattering (GIWAXS) for the in plane (IP) and out of plane (OOP) states by a CMOS flat panel X-ray detector (C9728DK).

3. Results and discussion

The functionalized and grafted CNTs and rGO nanosheets were prepared to deeply study their effect on the orientation of P3HT chains while crystallization onto the rGO surface. Three types of orientations including face-on, edge-on, and flat-on

were detected separately in various systems. When the bared CNT and rGO were utilized to develop the supramolecular donor-acceptor structures, the P3HT chains preferred to interact with their thiophene rings with the CNT and rGO surfaces (Figure 2). In these structures, a conventional face-on orientation was detected. The morphology of P3HT/CNT nano-hybrids was entitled as double-fibrillar (Figure 2(b)). The P3HT/rGO nano-hybrid structures developed in toluene within 6 h after filtration from the solution demonstrated a face-on orientation having the growth prisms of (002) in the backbone longitude and (100) in the hexyl side chains direction in the selected area electron diffraction (SAED) patterns. The fibrillar P3HT crystals having an edge-on orientation with the growth fronts of (020) in π-π stacking direction and (002) in the P3HT backbone longitude were constructed on the rGO during 20 h. Figure 2(a) shows TEM image accompanied by SAED pattern in the inset panel for P3HT/rGO supramolecule developed in toluene within 20 h. It was probable that further growth of P3HT nanofibrillar crystals in π-π stacking direction within a longer growth time led to the longer P3HT nanofibers on the rGO surface. After solvent evaporation, the P3HT
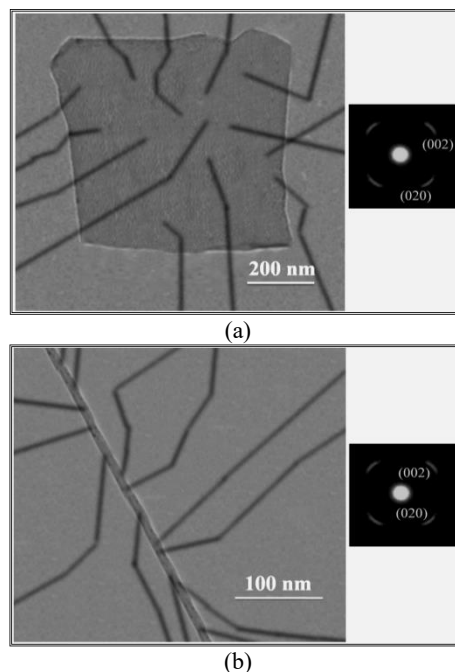

(a)

(b)

Fig. 2- TEM image with SAED pattern in the inset for P3HT/rGO supramolecule developed in toluene within 20 h (a); TEM image with SAED pattern in the inset panel for P3HT/CNT hybrid prepared in toluene within 20 h (b).

nanofibrils inclined onto the rGO surface, thereby the face-on orientation turned to the edge-on one. The face-on P3HTs having the alkyl chains parallel with the substrate depicted $(100)_{IP}$ and $(020)_{OOP}$ peaks (Figures 3(a) and (b)) and the edge-on P3HTs having the alkyl chains perpendicular to the substrate represented $(100)_{OOP}$ and $(020)_{IP}$ peaks (Figures 3(c) and (d)) in GIWAXS analyses.

As shown in Figure 4(a), for P3HT/rGO nano-hybrids, A_{0-2}, A_{0-1}, and A_{0-0} peaks in UV-Vis spectra appeared at about 475, 530, and 575 nm, respectively. For P3HT/CNT nano-hybrids, the characteristic peaks were detected at 478, 550, and 581 nm, respectively. The P3HT/CNT structures represented a small red-shift as well as a conspicuous enhancement in the peak intensities. The exciton diffusion efficiency was also examined by photoluminescence (PL) spectroscopy. The PL mainly occurs when the excitons recombine emissively before splitting [72]. The PL spectra were collected in the range of 550−900 nm. As depicted in Figure 4(b), a higher PL quenching was detected for the P3HT/CNT supramolecular structures, reflecting further growth of P3HT nanocrystals. A quenching in
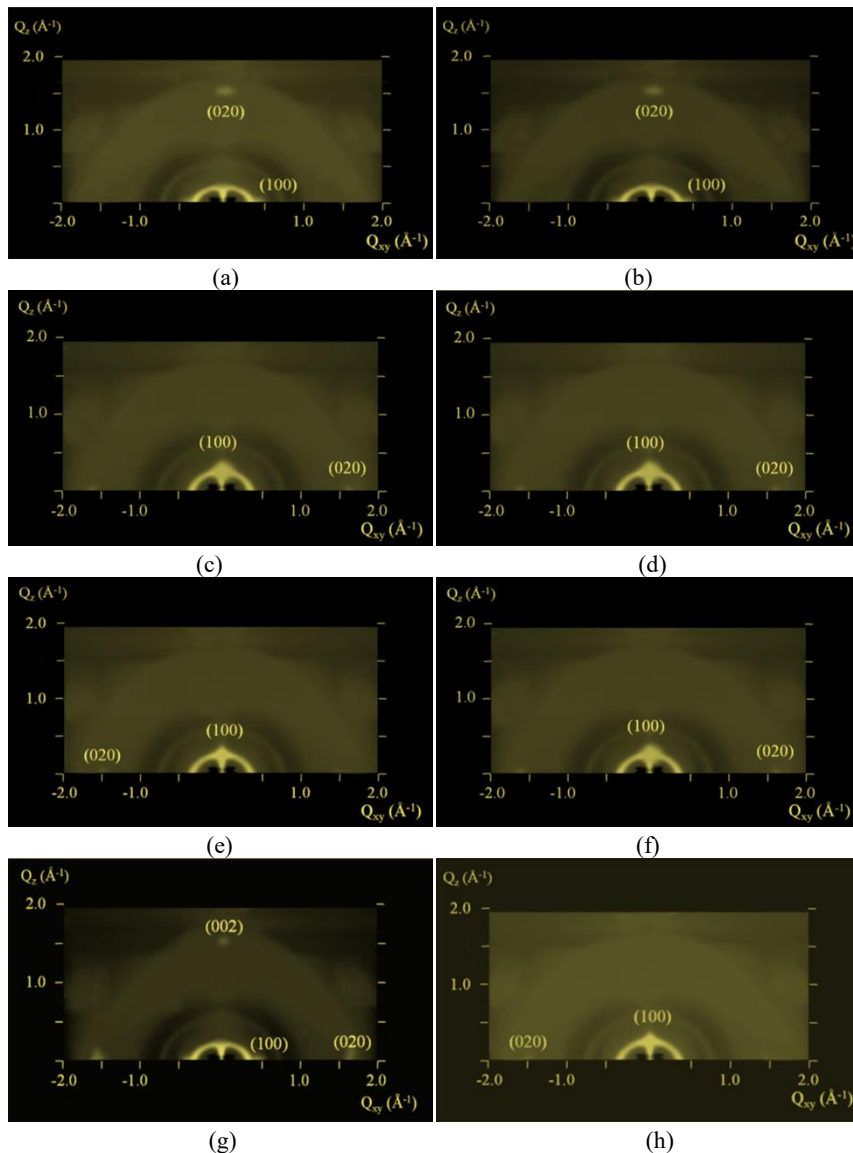

Fig. 3- GIWAXS plots of (a) short fibrillar P3HT/rGO with face-on orientation; (b) short fibrillar P3HT/CNT with face-on orientation; (c) long fibrillar CNT/P3HT with edge-on orientation; (d) long fibrillar rGO/P3HT with edge-on orientation; (e) shish-kebab P3HT/CNT-f-COOTh with edge-on orientation; (f) delicate patched sheet P3HT/rGO-f-TAA with edge-on orientation; (g) stem-leaf P3HT/CNT-g-PDDT with face-on orientation; (h) coarse patched sheet P3HT/rGO-g-PDDT with flat-on orientation.

the PL spectra intensity demonstrated the donor-acceptor nature of nano-hybrids.

By functionalizing the CNTs with 2-hydroxymethyl thiophene (CNT-f-COOTh) and rGOs with 2-thiophene acetic acid (rGO-f-TAA), the orientation of P3HT chains changed from face-on to edge-on with main backbones parallel with and hexyl side chains perpendicular to the CNT and rGO surfaces. This phenomenon was ascribed to the strong interactions between the hexyl side chains of P3HTs and functional groups. Actually, the attachment of P3HT chains changed from the thiophene rings directly onto the rGO or CNT surfaces to the interaction of hexyl side chains with functional groups. Regardless of the growth time and solvent quality, the edge-on orientation was dominant in all functionalized nano-hybrids. Figures 5(a) and (b) display TEM images accompanied by SAED pattern in the inset panels for P3HT/rGO-f-TAA and P3HT/CNT-f-COOTh supramolecules developed within 20 h, respectively. In these systems, the growth fronts of (020) in p-p stacking direction and (002) in the longitude of P3HT backbones appeared in SAED and $(100)_{OOP}$ and $(020)_{IP}$ peaks were also detected in GIWAXS

patterns, demonstrating an edge-on orientation (Figures 3(e) and (f)). The morphology acquired for the P3HT/rGO-f-TAA hybrids was a short fibrillar pattern composed of P3HT nanocrystals and called delicate patched sheet (Figure 5(a)). The dimensions of these short fibrillar P3HT crystals increased in the poorer solvents and also during the long periods of growth time. In P3HT/CNT-f-COOTh nano-hybrids, the shish (CNT-f-COOTh)-kebab (RR-P3HT) structures were originated, as depicted in Figure 5(b).

In UV-Vis spectra reported in Figure 6(a) for P3HT/rGO-f-TAA and P3HT/CNT-f-COOTh nano-hybrids a small red-shift (475, 540, and 590 nm) and also an increase in the peaks intensity were observed for CNT based supramolecules. Figure 6(b) also displays the PL spectra of respective supramolecular donor-acceptor structures. In conclusion, the face-on nano-hybrids demonstrated their identifying A_{0-2}, A_{0-1}, and A_{0-0} peaks at the higher wavelengths in UV-Vis spectra compared to the edge-on ones. In addition, the PL quenching further occurred in the face-on hybrids compared with the edge-on ones. The face-on orientation was a better orientation for the P3HT chains in the
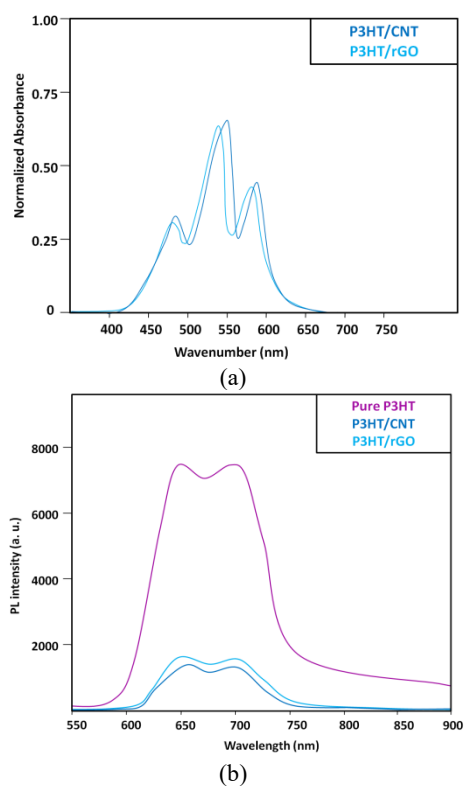

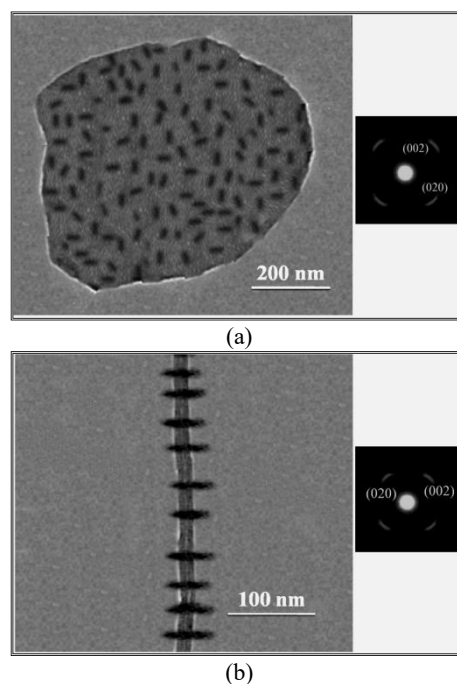Fig. 4- UV-Vis (a) and PL (b) spectra of P3HT/CNT and P3HT/rGO nano-hybrids.

Fig. 5- TEM image accompanied by SAED pattern in the inset panel for P3HT/rGO-f-TAA supramolecule developed in toluene within 20 h (a); TEM image accompanied by SAED pattern in the inset panel for P3HT/CNT-f-COOTh hybrid prepared in toluene within 20 h (b).

patterns onto the rGO.

The rGO surface was grafted with poly(3-dodecylthiophene) (rGO-g-PDDT) to manipulate the orientation and patterning of P3HTs. The surface of grafted rGO with poly(3-dodecylthiophene) was patterned by the rectangular patches composed of the flat-on oriented P3HT chains, in which the main backbones were perpendicular to the rGO surface. The growth prisms of (100) in the hexyl side chains direction and (020) in π-π stacking

direction were detected in SAED pattern of Figure 7(a). Irrespective of the solvent quality and growth period of time, the P3HT/rGO-g-PDDT supramolecular structures were patterned by the rectangular P3HT patches composed of flat-on backbones perpendicular to the rGO surface called coarse patched sheet. The dominant parameter in these systems was the grafting of rGO surface. In a deeper perspective, the grafted oligomers onto the rGO surface provoked the P3HT chains to attach perpendicularly onto the rGO, and develop the flat-on oriented rectangular patches. Arrangement
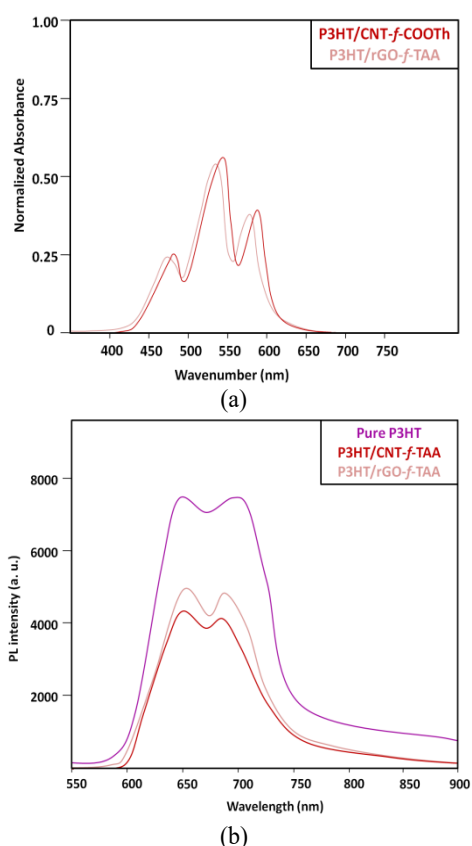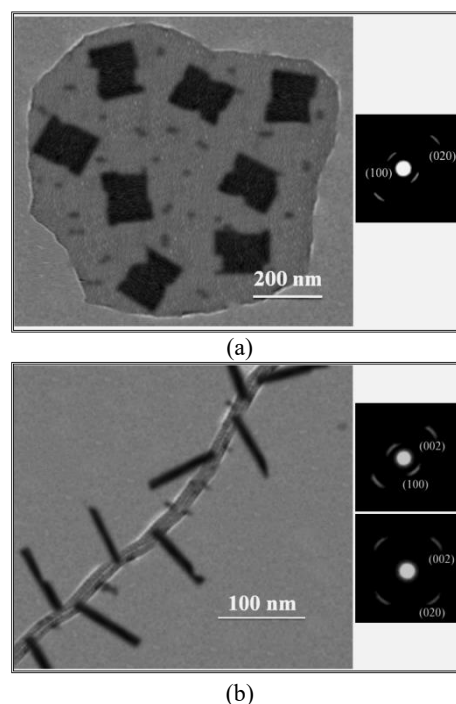

(a)

(b)

Fig. 7- TEM image accompanied by SAED pattern in the inset panel for P3HT/rGO-g-PDDT nano-hybrid developed in toluene within 20 h (a); TEM image accompanied by SAED pattern in the inset panel for P3HT/CNT-g-PDDT nano-hybrid prepared in toluene within 20 h (b).

(a)

(b)

Fig. 6- UV-Vis (a) and PL (b) spectra of P3HT/CNT-f-COOTh and P3HT/rGO-f-TAA nano-hybrids.

Table 1- The structural characteristics of different designed nano-hybrids

Sample	Morphology type	Orientation	Crystal scale (nm)
P3HT/CNT	double-fibrillar	face-on/edge-on	7−15
P3HT/CNT-*f*-COOTh	shish-kebab	edge-on	8−50
P3HT/CNT-*g*-PDDT	stem-leaf	flat-on	10−80
P3HT/rGO	fiber-sheet	face-on/edge-on	6−12
P3HT/rGO-*f*-TAA	Delicate patched sheet	edge-on	15−55
P3HT/rGO-*g*-PDDT	Coarse patched sheet	flat-on	90−210

of next P3HT backbones in the vicinity of attached chains gradually resulted in a patched-like pattern on the rGO-g-PDDT (Figure 3(g)).

When the surface of CNTs was grafted with PDDT, the stem (CNT-g-PDDT)-leaf (RR-P3HT) configurations were detected. The length of P3HT leaves was partly equal to the extended length of
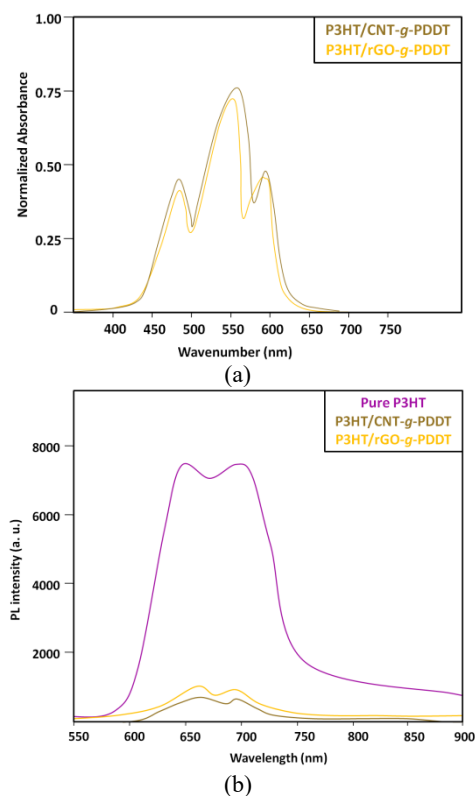

(a)

(b)

Fig. 8- UV-Vis (a) and PL (b) spectra of P3HT/CNT-g-PDDT and P3HT/rGO-g-PDDT nano-hybrids.

Table 2- The electrical conductivity values of different nano-hybrids

Sample	Run 1 (S/cm)	Run 2 (S/cm)	Run 3 (S/cm)
CNT	4.15	4.13	4.16
P3HT/CNT	5.13	5.14	5.18
CNT-f-COOTh	0.57	0.59	0.58
P3HT/CNT-f-COOTh	2.24	2.19	2.20
CNT-g-PDDT	2.89	2.89	2.84
P3HT/CNT-g-PDDT	7.50	7.45	7.39
rGO	0.33	0.35	0.30
P3HT/rGO	3.87	3.81	3.84
rGO-f-TAA	0.56	0.58	0.59
P3HT/rGO-f-TAA	3.95	3.94	3.91
rGO-g-PDDT	1.38	1.35	1.38
P3HT/rGO-g-PDDT	10.67	10.70	10.69

P3HT chains having the molecular weight of 30 KDa (75 nm). This phenomenon was detected in all growth systems with either toluene of DMF. The variation in the preparation time (2 to 20 h) did not also change the length of P3HT leaves (75 nm). Indeed, the RR-P3HT chains were extendedly attached to the CNT-g-PDDT surface, albeit with the help of PDDT grafts. After solvent evaporation, the P3HT leaves were inclined onto the substrate with either edge-on or face-on (insets of Figure 7(b) and Figure 3(h)) orientations. The structural properties of designed nano-hybrids are tabulated in Table 1. The conductivity values of supramolecular nanostructures are also reported in Table 2.

The UV-Vis spectra of supramolecular structures are reported in Figure 8(a). The A_{0-2}, A_{0-1}, and A_{0-0} peaks appeared at around 480, 544, and 588 nm for P3HT/rGO-g-PDDT nano-hybrids and at around 482, 556, and 590 nm for P3HT/CNT-g-PDDT supramolecules. Figure 8(b) also represents the corresponding PL spectra. The higher quenching in the PL spectra was a fingerprint of the stronger donor-acceptor supramolecular structures. As an interesting point, the UV-Vis spectra of P3HT/CNT-g-PDDT and P3HT/rGO-g-PDDT supramolecules demonstrated the most intensified A_{0-2}, A_{0-1}, and A_{0-0} peaks, and also the highest red-shifting. The flat-on chains having the backbones perpendicular to the substrate resulted in the highest conductivity and hole mobility. The highest quenching values in the PL spectra were detected for P3HT/CNT-g-PDDT and P3HT/rGO-g-PDDT structures.

4. Conclusions

Different nano-hybrids with double-fibrillar, shish-kebab, and stem-leaf configurations were prepared for the unmodified, functionalized, and grafted CNTs using regioregular P3HTs. The functionalized (rGO-f-TAA) and grafted (rGO-g-PDDT) rGO nanosheets were also prepared to investigate the differences in CNT and rGO nano-hybrids. The most effective parameter on the morphology and orientation of donor-acceptor nano-hybrids was the chemical modification of surface. The fibrillar morphology and face-on orientation of P3HT assemblies were detected onto unmodified CNT and rGO nanostructures. The shish-kebab and nanocrystal decorated configurations were obtained for functionalized CNT and rGO, respectively; however, the

orientation of P3HT chains was edge-on in both of them. In CNT-g-PDDT/P3HT and rGO-g-PDDT/P3HT nanostructures, the P3HT chains were extendedly assembled onto the grafted carbonic materials, whereas their different natures led to the stem-leaf and patched morphologies, respectively. The flat-on orientation reached for CNT-g-PDDT/P3HT and rGO-g-PDDT/P3HT systems was the best for P3HT assemblies.

References

1. Acevedo-Cartagena DE, Zhu J, Trabanino E, Pentzer E, Emrick T, Nonnenmann SS, et al. Selective Nucleation of Poly(3-hexyl thiophene) Nanofibers on Multilayer Graphene Substrates. ACS Macro Letters. 2015;4(5):483-7.

2. Yang Z, Lu H. Nonisothermal crystallization behaviors of poly(3-hexylthiophene)/reduced graphene oxide nanocomposites. Journal of Applied Polymer Science. 2012;128(1):802-10.

3. Skrypnychuk V, Boulanger N, Yu V, Hilke M, Mannsfeld SCB, Toney MF, et al. Enhanced Vertical Charge Transport in a Semiconducting P3HT Thin Film on Single Layer Graphene. Advanced Functional Materials. 2014;25(5):664-70.

4. Wang G, Swensen J, Moses D, Heeger AJ. Increased mobility from regioregular poly(3-hexylthiophene) field-effect transistors. Journal of Applied Physics. 2003;93(10):6137-41.

5. Yang H, Shin TJ, Yang L, Cho K, Ryu CY, Bao Z. Effect of Mesoscale Crystalline Structure on the Field-Effect Mobility of Regioregular Poly(3-hexyl thiophene) in Thin-Film Transistors. Advanced Functional Materials. 2005;15(4):671-6.

6. Surin M, Leclère P, Lazzaroni R, Yuen JD, Wang G, Moses D, et al. Relationship between the microscopic morphology and the charge transport properties in poly(3-hexylthiophene) field-effect transistors. Journal of Applied Physics. 2006;100(3):033712.

7. Gargi D, Kline RJ, DeLongchamp DM, Fischer DA, Toney MF, O'Connor BT. Charge Transport in Highly Face-On Poly(3-hexylthiophene) Films. The Journal of Physical Chemistry C. 2013;117(34):17421-8.

8. Jimison LH, Himmelberger S, Duong DT, Rivnay J, Toney MF, Salleo A. Vertical confinement and interface effects on the microstructure and charge transport of P3HT thin films. Journal of Polymer Science Part B: Polymer Physics. 2013;51(7):611-20.

9. Porzio W, Scavia G, Barba L, Arrighetti G, Milita S. Depth-resolved molecular structure and orientation of polymer thin films by synchrotron X-ray diffraction. European Polymer Journal. 2011;47(3):273-83.

10. Geim AK, Novoselov KS. The rise of graphene. Nature Materials. 2007;6(3):183-91.

11. Novoselov KS, Morozov SV, Mohinddin TMG, Ponomarenko LA, Elias DC, Yang R, et al. Electronic properties of graphene. physica status solidi (b). 2007;244(11):4106-11.

12. Mihailetchi VD, van Duren JKJ, Blom PWM, Hummelen JC, Janssen RAJ, Kroon JM, et al. Electron Transport in a Methanofullerene. Advanced Functional Materials. 2003;13(1):43-6.

13. Kim DH, Lee HS, Shin H-J, Bae Y-S, Lee K-H, Kim S-W, et al. Graphene surface induced specific self-assembly of poly(3-hexylthiophene) for nanohybrid optoelectronics: from first-principles calculation to experimental characterizations. Soft Matter. 2013;9(22):5355.

14. Zhang Y, Tan Y-W, Stormer HL, Kim P. Experimental observation of the quantum Hall effect and Berry's phase in graphene. Nature. 2005;438(7065):201-4.

15. Novoselov KS. Electric Field Effect in Atomically Thin Carbon Films. Science. 2004;306(5696):666-9.

16. Pang S, Hernandez Y, Feng X, Müllen K. Graphene as Transparent Electrode Material for Organic Electronics. Advanced Materials. 2011;23(25):2779-95.

17. Gomez De Arco L, Zhang Y, Schlenker CW, Ryu K, Thompson ME, Zhou C. Continuous, Highly Flexible, and Transparent Graphene Films by Chemical Vapor Deposition for Organic Photovoltaics. ACS Nano. 2010;4(5):2865-73.

18. Liu W, Jackson BL, Zhu J, Miao C-Q, Chung C-H, Park YJ, et al. Large Scale Pattern Graphene Electrode for High Performance in Transparent Organic Single Crystal Field-Effect Transistors. ACS Nano. 2010;4(7):3927-32.

19. Kang SJ, Kim B, Kim KS, Zhao Y, Chen Z, Lee GH, et al. Inking Elastomeric Stamps with Micro-Patterned, Single Layer Graphene to Create High-Performance OFETs. Advanced Materials. 2011;23(31):3531-5.

20. Yu WJ, Lee SY, Chae SH, Perello D, Han GH, Yun M, et al. Small Hysteresis Nanocarbon-Based Integrated Circuits on Flexible and Transparent Plastic Substrate. Nano Letters. 2011;11(3):1344-50.

21. Kim KS, Zhao Y, Jang H, Lee SY, Kim JM, Kim KS, et al. Large-scale pattern growth of graphene films for stretchable transparent electrodes. Nature. 2009;457(7230):706-10.

22. Choi D, Choi M-Y, Choi WM, Shin H-J, Park H-K, Seo J-S, et al. Fully Rollable Transparent Nanogenerators Based on Graphene Electrodes. Advanced Materials. 2010;22(19):2187-92.

23. Huang G, Hou C, Shao Y, Wang H, Zhang Q, Li Y, et al. Highly Strong and Elastic Graphene Fibres Prepared from Universal Graphene Oxide Precursors. Scientific Reports. 2014;4(1).

24. Joshi RK, Carbone P, Wang FC, Kravets VG, Su Y, Grigorieva IV, et al. Precise and Ultrafast Molecular Sieving Through Graphene Oxide Membranes. Science. 2014;343(6172):752-4.

25. Wang L, Meric I, Huang PY, Gao Q, Gao Y, Tran H, et al. One-Dimensional Electrical Contact to a Two-Dimensional Material. Science. 2013;342(6158):614-7.

26. Chunder A, Liu J, Zhai L. Reduced Graphene Oxide/Poly(3-hexylthiophene) Supramolecular Composites. Macromolecular Rapid Communications. 2010;31(4):380-4.

27. Zhou X, Chen Z, Qu Y, Su Q, Yang X. Fabricating graphene oxide/poly(3-butylthiophene) hybrid materials with different morphologies and crystal structures. RSC Advances. 2013;3(13):4254.

28. Lightcap IV, Kamat PV. Graphitic Design: Prospects of Graphene-Based Nanocomposites for Solar Energy Conversion, Storage, and Sensing. Accounts of Chemical Research. 2012;46(10):2235-43.

29. Li S-S, Tu K-H, Lin C-C, Chen C-W, Chhowalla M. Solution-Processable Graphene Oxide as an Efficient Hole Transport Layer in Polymer Solar Cells. ACS Nano. 2010;4(6):3169-74.

30. Gao Y, Yip H-L, Chen K-S, O'Malley KM, Acton O, Sun Y, et al. Surface Doping of Conjugated Polymers by Graphene Oxide and Its Application for Organic Electronic Devices. Advanced Materials. 2011;23(16):1903-8.

31. Liu X, Kim H, Guo LJ. Optimization of thermally reduced graphene oxide for an efficient hole transport layer in polymer solar cells. Organic Electronics. 2013;14(2):591-8.

32. Wang Q, Cui X, Chen J, Zheng X, Liu C, Xue T, et al. Well-dispersed palladium nanoparticles on graphene oxide as a non-enzymatic glucose sensor. RSC Advances. 2012;2(15):6245.

33. Schedin F, Geim AK, Morozov SV, Hill EW, Blake P, Katsnelson MI, et al. Detection of individual gas molecules adsorbed on graphene. Nature Materials. 2007;6(9):652-5.

34. Choi BG, Park H, Park TJ, Yang MH, Kim JS, Jang S-Y, et al. Solution Chemistry of Self-Assembled Graphene Nanohybrids for High-Performance Flexible Biosensors. ACS Nano. 2010;4(5):2910-8.

35. Huang L, Huang Y, Liang J, Wan X, Chen Y. Graphene-based conducting inks for direct inkjet printing of flexible conductive patterns and their applications in electric circuits and chemical sensors. Nano Research. 2011;4(7):675-84.

36. Obradovic B, Kotlyar R, Heinz F, Matagne P, Rakshit T, Giles MD, et al. Analysis of graphene nanoribbons as a channel material for field-effect transistors. Applied Physics Letters. 2006;88(14):142102.

37. Liu Z, Liu Q, Huang Y, Ma Y, Yin S, Zhang X, et al. Organic Photovoltaic Devices Based on a Novel Acceptor Material: Graphene. Advanced Materials. 2008;20(20):3924-30.

38. Bonaccorso F, Sun Z, Hasan T, Ferrari AC. Graphene photonics and optoelectronics. Nature Photonics. 2010;4(9):611-22.

39. Ramanathan T, Abdala AA, Stankovich S, Dikin DA, Herrera-Alonso M, Piner RD, et al. Functionalized graphene sheets for polymer nanocomposites. Nature Nanotechnology. 2008;3(6):327-31.

40. Watcharotone S, Dikin DA, Stankovich S, Piner R, Jung I, Dommett GH, Evmenenko G, Wu SE, Chen SF, Liu CP, Nguyen ST. Graphene− silica composite thin films as transparent conductors. Nano letters. 2007 Jul 11;7(7):1888-92.

41. Li G, Shrotriya V, Huang J, Yao Y, Moriarty T, Emery K, et al. High-efficiency solution processable polymer photovoltaic cells by self-organization of polymer blends. Nature Materials. 2005;4(11):864-8.

42. Zhou X, Yang X. Improved dispersibility of graphene oxide in o-dichlorobenzene by adding a poly(3-alkylthiophene). Carbon. 2012;50(12):4566-72.

43. Kausar A. A Study on Poly(vinyl alcohol-co-ethylene)-graft-Polystyrene Reinforced with Two Functional Nanofillers. Polymer-Plastics Technology and Engineering. 2015;54(7):741-9.

44. Lu R, Christianson C, Kirkeminde A, Ren S, Wu J. Extraordinary Photocurrent Harvesting at Type-II Heterojunction Interfaces: Toward High Detectivity Carbon Nanotube Infrared Detectors. Nano Letters. 2012;12(12):6244-9.

45. Kanai Y, Grossman JC. Role of Semiconducting and Metallic Tubes in P3HT/Carbon-Nanotube Photovoltaic Heterojunctions: Density Functional Theory Calculations. Nano Letters. 2008;8(3):908-12.

46. Schuettfort T, Nish A, Nicholas RJ. Observation of a Type II Heterojunction in a Highly Ordered Polymer−Carbon Nanotube Nanohybrid Structure. Nano Letters. 2009;9(11):3871-6.

47. Hughes M, Chen GZ, Shaffer MSP, Fray DJ, Windle AH. Electrochemical Capacitance of a Nanoporous Composite of Carbon Nanotubes and Polypyrrole. Chemistry of Materials. 2002;14(4):1610-3.

48. Bandyopadhyaya R, Nativ-Roth E, Regev O, Yerushalmi-Rozen R. Stabilization of Individual Carbon Nanotubes in Aqueous Solutions. Nano Letters. 2002;2(1):25-8.

49. Riggs JE, Guo Z, Carroll DL, Sun Y-P. Strong Luminescence of Solubilized Carbon Nanotubes. Journal of the American Chemical Society. 2000;122(24):5879-80.

50. Hill DE, Lin Y, Rao AM, Allard LF, Sun Y-P. Functionalization of Carbon Nanotubes with Polystyrene. Macromolecules. 2002;35(25):9466-71.

51. Ebbesen TW, Lezec HJ, Hiura H, Bennett JW, Ghaemi HF, Thio T. Electrical conductivity of individual carbon nanotubes. Nature. 1996;382(6586):54-6.

52. Ruoff RS, Qian D, Liu WK. Mechanical properties of carbon nanotubes: theoretical predictions and experimental measurements. Comptes Rendus Physique. 2003;4(9):993-1008.

53. Javey A, Guo J, Wang Q, Lundstrom M, Dai H. Ballistic carbon nanotube field-effect transistors. Nature. 2003;424(6949):654-7.

54. Snow ES. Chemical Detection with a Single-Walled Carbon Nanotube Capacitor. Science. 2005;307(5717):1942-5.

55. Sahoo S, Husale S, Karna S, Nayak SK, Ajayan PM. Controlled Assembly of Ag Nanoparticles and Carbon Nanotube Hybrid Structures for Biosensing. Journal of the American Chemical Society. 2011;133(11):4005-9.

56. Wang X, Wang C, Cheng L, Lee S-T, Liu Z. Noble Metal Coated Single-Walled Carbon Nanotubes for Applications in Surface Enhanced Raman Scattering Imaging and Photothermal Therapy. Journal of the American Chemical Society. 2012;134(17):7414-22.

57. Qiu W, Li Q, Lei Z-K, Qin Q-H, Deng W-L, Kang Y-L. The use of a carbon nanotube sensor for measuring strain by micro-Raman spectroscopy. Carbon. 2013;53:161-8.

58. Xie X, Mai Y, Zhou X. Dispersion and alignment of carbon nanotubes in polymer matrix: A review. Materials Science and Engineering: R: Reports. 2005;49(4):89-112.

59. De Volder MFL, Tawfick SH, Baughman RH, Hart AJ. Carbon Nanotubes: Present and Future Commercial Applications. Science. 2013;339(6119):535-9.

60. Andrews R, Jacques D, Qian D, Rantell T. Multiwall Carbon Nanotubes: Synthesis and Application. Accounts of Chemical Research. 2002;35(12):1008-17.

61. Liu IC, Huang H-M, Chang C-Y, Tsai H-C, Hsu C-H, Tsiang RC-C. Preparing a Styrenic Polymer Composite Containing Well-Dispersed Carbon Nanotubes: Anionic Polymerization of a Nanotube-Boundp-Methylstyrene. Macromolecules. 2004;37(2):283-7.

62. Kong H, Gao C, Yan D. Controlled Functionalization of Multiwalled Carbon Nanotubes by in Situ Atom Transfer Radical Polymerization. Journal of the American Chemical Society. 2004;126(2):412-3.

63. Zhao B, Hu H, Haddon RC. Synthesis and Properties of a Water-Soluble Single-Walled Carbon Nanotube–Poly(m-aminobenzene sulfonic acid) Graft Copolymer. Advanced Functional Materials. 2004;14(1):71-6.

64. Hsiao C-C, Lin TS, Cheng LY, Ma C-CM, Yang ACM. The Nanomechanical Properties of Polystyrene Thin Films Embedded with Surface-grafted Multiwalled Carbon Nanotubes. Macromolecules. 2005;38(11):4811-8.

65. Lin CW, Huang LC, Ma CCM, Yang ACM, Lin CJ, Lin LJ. Nanoplastic Flows of Glassy Polymer Chains Interacting with Multiwalled Carbon Nanotubes in Nanocomposites. Macromolecules. 2008;41(13):4978-88.

66. Lin C-W, Yang ACM. Nanoplastic Interactions of Surface-Grafted Single-Walled Carbon Nanotubes with Glassy Polymer Chains in Nanocomposites. Macromolecules. 2010;43(16):6811-7.

67. Karim MR, Yeum JH, Lee MS, Lim KT. Synthesis of conducting polythiophene composites with multi-walled carbon nanotube by the γ-radiolysis polymerization method. Materials Chemistry and Physics. 2008;112(3):779-82.

68. Robertson J. Realistic applications of CNTs. Materials Today. 2004;7(10):46-52.

69. Yu K, Lee JM, Kim J, Kim G, Kang H, Park B, et al. Semiconducting Polymers with Nanocrystallites Interconnected via Boron-Doped Carbon Nanotubes. Nano Letters. 2014;14(12):7100-6.

70. Mozaffari S, Li W, Thompson C, Ivanov S, Seifert S, Lee B, et al. Colloidal nanoparticle size control: experimental and kinetic modeling investigation of the ligand–metal binding role in controlling the nucleation and growth kinetics. Nanoscale. 2017;9(36):13772-85.

71. Jing C, Rawson FJ, Zhou H, Shi X, Li W-H, Li D-W, et al. New Insights into Electrocatalysis Based on Plasmon Resonance for the Real-Time Monitoring of Catalytic Events on Single Gold Nanorods. Analytical Chemistry. 2014;86(11):5513-8.

72. Cates NC, Gysel R, Beiley Z, Miller CE, Toney MF, Heeney M, et al. Tuning the Properties of Polymer Bulk Heterojunction Solar Cells by Adjusting Fullerene Size to Control Intercalation. Nano Letters. 2009;9(12):4153-7.